Determination of the aperture distribution of rough-walled rock fractures with the non-toxic Yield Stress fluids porosimetry method

Antonio Rodríguez de Castro [a,*], Azita Ahmadi-Sénichault [b], Abdelaziz Omari [c]

[a] *Arts et Metiers Institute of Technology, MSMP, HESAM Université, F-51006 Châlons-en-Champagne, France*
[b] *Arts et Metiers Institute of Technology, Université de Bordeaux, CNRS, INRA, INP, HESAM Université, F-33405 Talence, France*
[c] *I2M, Bordeaux-INP, CNRS, Esplanade des Arts et Métiers, 33405 TalenceCedex, France*

Fractures in geological formations constitute high-conductivity conduits which potentially act as preferential paths during fluid injection in soil remediation and reservoir engineering operations. Recently, the measurement of the pressure drop under different flow rates during the flow of yield stress fluids in porous media has been proposed as the basis for an environmentally friendly method to characterize the Pore Size Distribution. However, the Yield Stress fluids porosimetry Method (YSM) has still not been extended to the characterization of the hydraulic aperture distribution of rough-walled rock fractures. The potential interest of such an extension is intense, considering that the distinct characteristics of rock fractures vs the matrix represent a burden to other traditional porosimetry techniques. In the particular case of X-ray microtomography, time-consuming calibration is often needed, and serious difficulties arise due to beam hardening and reconstruction artifacts. The specific objective of the present investigation is to adapt YSM to the characterization of rough-walled rock fractures. For this purpose, the results of laboratory experiments in which a yield stress fluid was injected through two natural rock fractures were exploited, and the YSM model and algorithm was adapted to the particular topological and geometrical features of flows in fractures. Moreover, numerical experiments were performed at the scale of a single 2D channel with variable aperture to identify the dimension characterized by YSM and decipher the yielding behaviour of the fluids. The present findings show that YSM can be successfully used to characterize the distribution of hydraulic apertures of the flow channels in rough-walled rock fractures. Furthermore, the numerical results revealed that the plug of stagnant fluid is located in the central part of these flow channels and breaks close to the constrictions, forming islands of unyielded fluid.

1. Introduction

Flow through fractured porous media plays a major role in various fields of geosciences, including reservoir exploitation for water supply, transport of contaminants from subsurface repositories, geological isolation of nuclear waste, underground storage of CO_2, mineralization processes, mining, petroleum engineering and geothermal systems (Berkowitz, 2002; Berre et al., 2019; Javadi et al., 2010). Given that the permeability of the fracture is orders of magnitude higher than that of the rock in which it is formed, the fracture acts as a high-conductivity conduit from the surrounding reservoir towards the producing well in Enhanced Oil Recovery. Among other applications, this raises a central issue in the specific case of soil remediation operations, in which the displacing liquid may bypass the contaminated matrix if a natural fracture network is hit during injection (Lavrov, 2013a). A great number of yield stress fluids are commonly used as both displacing fluids to enhance mobility ratio and blocking agents to divert flow from highly permeable regions, e.g., polymer solutions, slurries, foams and microemulsion(Kovscek and Bertin, 2003; Silva et al., 2012; Di Cristo et al., 2019; Forey et al., 2020; Omirbekov et al., 2020). Consequently, it is of crucial importance to understand the flow behaviour of yield stress fluids as they enter fractures that are rough-walled by nature. On

this subject, Frigaard et al. (2017) reviewed the extensive use of yield stress fluids in oil and gas industry, including the flow through fractured media. As reviewed by Birdsell et al. (2015), hydraulic fracturing is a source of environmental concern due, among other issues, to the potential upward migration of the fracturing fluids to shallow drinking water aquifers through permeable pathways such as existing fractures. Such fracturing fluids often exhibit a yield stress, therefore generating extra motivation for investigating the flow of yield stress fluids in fractured media.

Fracture wall surfaces are rough and do not perfectly match, generating voids of different sizes and spatial heterogeneity of the flow field (Auradou et al., 2006). For this reason, the accurate evaluation of fracture hydro-mechanical properties relies heavily on the knowledge of the Aperture Distribution (AD), i.e., the distribution of perpendicular distances between asperities on adjacent fracture surfaces which serve as fluid flow paths (Dang et al., 2019; Li et al., 2020). By analogy with a homogeneous porous medium, the AD of the fracture can be considered as being its Pore Size Distribution (PSD), as the flow channels of varying aperture can be assimilated to individual pores.

Huo et al. (2016) listed 10 methods for measuring fracture apertures, together with their main advantages and drawbacks, as presented in Table 1. Among these methods, the popular non-destructive computed

* Corresponding author at: Arts et Métiers Institute of Technology, Rue Saint-Dominique, 51006 Châlons-en-Champagne, France
E-mail address: antonio.rodriguezdecastro@ensam.eu (A. Rodríguez de Castro).

Table 1
Methods for measuring fracture apertures. From Huo et al. (2016).

Methods	Mechanism	Advantages	Drawbacks	References
Mechanical profilometer	Surface profilometry	High resolution	Destructive method	Glover et al. (1998)
Optical methods	Surface profilometry	High resolution	Destructive method	Isakov et al. (2001)
Laser profilometer	Surface profilometry	High resolution	Destructive method	Boutt et al. (2006)
Tapered filler gauge	Material filling	Easy to measure	Cannot obtain local aperture distribution	Bandis (1980)
Polyester film	Material filling	Good estimates of local aperture geometry	Destructive method; overestimates the contact area	Committee on Fracture Characterization and Fluid Flow et al. (1996)
Epoxy	Material filling	Local aperture and void distribution can be obtained	Destructive method	Gale (1987); Billaux and Gentier (1990)
Wood's metal	Material filling	Estimates of areal distribution of void space	Difficult to obtain local aperture geometry	Pyrak-Nolte et al. (1987)
Gas volume measurements	Material filling	Easy to set up experiments	Cannot obtain aperture distribution	Schrauf and Evans (1986)
Borehole pumping tests	Material filling	Easy method in large fractures	Equals mechanical aperture with hydraulic aperture	Barton et al. (1985)
Computed tomography scanning	Noninfiltrative	"In-situ" experiments and can be combined with flow experiments	Resolution limitations	Ketcham and Carlson (2001)

tomography method presents the serious shortcoming of needing calibration (Johns et al., 1993; Weerakone and Wong ,2010; Lai et al., 2017) in its conventional version, which is a time-consuming task and generally difficult to achieve on fracture networks (Voorn et al., 2015). Moreover, the use of X-ray micro-computed tomography tests to characterize the PSD of fractured media is challenging, given the disparity between the dimensions of the fracture apertures and the size of the pores in the rock (Li et al., 2017). Indeed, different requirements in terms of spatial resolution need to be met for the fracture and the host rock. Also, the thin samples that are used in X-ray micro-computed tomography may not be representative of the heterogeneity of fractured media. A great number of previous works exist dealing with the application of X-ray to characterize the microstructure of porous media, and the details on the advantages and limitations of this technique can be consulted in the literature (Lindquist and Venkatarangan, 2000; Burlion et al., 2006; Prodanovic et al., 2006; Karpyn et al., 2007; Wildenschild and Sheppard, 2012; Bultreys et al., 2016; Li et al., 2017; Houston et al., 2017; Tembely et al., 2019). Regarding the methods for fracture aperture characterization based on surface topography measurements, resin injection and casting techniques, Hakami et al. (1995) presented a review in which the advantages and shortcomings of each method were critically discussed. As explained by these authors, the preceding methods are intended for research purposes, as in field mapping for site characterisation the measurements must be quicker and simpler.

The injection of yield stress fluids in porous media was first proposed as a potential method for porosimetry by Ambari et al. (1990). In that work, it was shown that the PSD of porous media can be derived from the measurement of flow rate Q vs. pressure gradient ∇P during injection of a yield stress fluid through a sample of the investigated material. The medium was modelled as an equivalent bundle of straight cylindrical capillaries of circular cross section with different radii providing the same flow rate vs. pressure gradient relationship as the actual sample. Although the method was first proposed only for Bingham fluids, it was extended to Casson and Herschel-Bulkley fluids in subsequent works (Oukhlef, 2011; Oukhlef et al., 2014). Moreover, Oukhlef et al. (2014) performed a set of numerical experiments with yield stress fluids in which the PSDs of bundles of capillaries were successfully computed from the analytical inversion of the generated Q vs. ∇P datasets. Some major drawbacks of such inversion procedure were its deep sensitivity to experimental uncertainty and the noisy results obtained in the small pore size region. In an attempt to solve these issues, Malvault (2013) proposed a procedure to achieve numerical inversion of Q vs. ∇P data obtained from laboratory experiments. Nevertheless, the accuracy of the results was highly dependent on the choice of

the order of the polynomial fitting required to invert the experimental data.

The preceding contributions and theoretical concepts constituted the starting point for the development of the Yield Stress porosimetry Method (YSM), which was presented by (Rodríguez de Castro et al., 2014) as a clean alternative to toxic Mercury Intrusion Porosimetry (León y León, 1998; Giesche, 2006; Cieszko et al., 2019). The inversion algorithm followed in YSM uses the raw experimental data as input, without any filtering or interpolation. This was accomplished by identifying the contribution in terms of flow rate occurring only in the pores of decreasing size in which the fluid yields when the pressure gradient is steeply increased. Then, from this new contribution, the number of pores of the incorporated pore size class can be determined. YSM was successfully applied to characterize the PSDs of both synthetic and natural consolidated porous media (Rodríguez de Castro et al., 2016; 2018). More recently, Rodríguez de Castro et al. (2019) characterized the PSDs of unconsolidated packs of spherical beads by using YSM. The preceding work showed that the results of YSM were essentially identical to those provided by Mercury Intrusion Porosimetry. Also, the comparison of YSM results with pore network models proved that the pore dimension being characterized by YSM is closer to the pore constriction rather than the pore body. However, rough-walled fractures constitute a distinct type of pores given that the distance between the walls of the fracture, i.e. the aperture, is much lower than the width and the length of the fracture. Moreover, in many fractures, both walls come into contact (zero aperture) only at a limited number of points. Consequently, the interstices are composed of a set of wide pores with varying aperture in-between the contact points rather than being a network of interconnected smaller pores as is the case in common porous media such as rocks or sand packs. For this reason, the bundle-of-cylindrical-capillaries model used when applying YSM to traditional porous media needs to be adapted to the geometrical and topological particularities of fractures.

The previous contributions to the development of a method to characterize the pore size distributions of porous media through the injection of complex fluids are summarized in the supplementary material of the present article (Table S1). Until now, YSM has only been applied to isotropic porous media. The objective of the present investigation is to extend the use of YSM to the characterization of rough-walled rock fractures in terms of their Hydraulic Aperture Distribution (HAD). In order to fulfil this objective, a model is first proposed to provide a suitable representation of the flow of yield stress fluids through this particular porous structure. Then, a set of previously published experiments in which a yield stress fluid is injected through two replicas of real

rock fractures are used as input to YSM algorithm in order to obtain the HAD. Additionally, several 2D numerical simulations are performed to gain further insight into the characteristic aperture controlling the generation of pressure losses, and therefore the YSM measurements, in fractures. The conclusions of the current study are critically discussed, allowing the evaluation of YSM as an efficient method to characterize rough-walled rock fractures.

2. Application of Yield Stress fluids porosimetry Method to rough-walled rock fractures

In this section, the porous medium model and the fluid rheology considered in the extension of YSM method to rough-walled rock fractures are presented, together with the underlying assumptions and the algorithm used to extract the HAD.

2.1. Modelling the flow of yield stress fluids through rough fractures

The steady-state shear rheology of the yield stress fluids used in the YSM method is described by Herschel-Bulkley's law (Eq. 1), under the assumption of simple shear conditions:

$$\begin{cases} \tau = \tau_0 + k\dot{\gamma}^n \text{ for } \tau \geq \tau_0 \\ \dot{\gamma} = 0 \text{ for } \tau \leq \tau_0 \end{cases} \tag{1}$$

In this model, τ_0 is the yield stress, k is the consistency and n is the power-law index of the fluid. These rheological parameters are determined by fitting τ vs $\dot{\gamma}$ data obtained with a controlled-stress rheometer. Neuzil and Tracy (1981), Tsang and Tsang (1987) and Silliman (1989) proposed simplified fracture models with 1-D aperture variability in which the total Newtonian flow through a rough-walled fracture is considered to be the sum of a set of elementary flows through plate channels of different apertures. This type of model was subsequently extended to power-law fluid flows (di Federico, 1998) and, more recently, to the flow of truncated power-law fluids (Felisa et al., 2018). Using a similar approach, Auradou et al. (2006) presented a simple model in which the aperture field is replaced by a set of parallel channels, each of constant aperture and perpendicular to the direction of shear displacement in shear-displaced fractures exhibiting self-affine geometries. In the preceding work, the authors showed that for a mean flow parallel to these channels, the fluid streamlines are only weakly tortuous and the variations in their velocity along these flow paths are small compared to the velocity contrasts from one channel to another. For each channel the velocity of the fluid was related to the pressure gradient by Darcy's equation. In a subsequent work (Auradou et al., 2008), the width and geometry of the front of a dyed shear-thinning polymer solution displacing a transparent solution of the same composition were studied as a function of the fluid rheology and flow rate, observing low transverse mixing between the flow paths and showing hence that the fracture could be considered as a set of parallel ducts of constant hydraulic apertures. Also, their results showed that the flow velocity contrasts between different flow channels was more significant for shear-thinning fluids than for Newtonian fluids. The Newtonian hydraulic aperture of a rough-walled fracture h_N is defined as the aperture of a Hele-Shaw cell producing the same pressure loss as the actual rough-walled fracture under any flow rate for the injection of a Newtonian fluid.

Therefore, in the model used in the current work, the void space between the walls of a rough fracture is discretized in a bundle of Z straight parallel flow channels with rectangular cross-section of widths w_i and apertures h_i (with i ranging from 1 to Z). A schematic representation of this model is provided in Fig. 1. The transverse flow between channels may be considered as negligible (Auradou et al., 2008). Therefore, one-dimensional flow is considered within each flow channel, the wall-effects are neglected over the width direction, and slipping condition is assumed between neighbour flow channels, as displayed in Fig. 1(c). In this regard, Lavrov (2013b) numerically showed that a strong channelization of the flow occurs during the injection of shear-thinning fluids

through rough-walled fractures. This means that the flow rate contribution in the direction of the applied pressure gradient is much larger than the flow rate contribution perpendicular to the global direction of the flow, as a consequence of the very high effective viscosity values exhibited by this type of fluids at small pressure gradients.

It is to be noted that such a simple model is not expected to represent the actual geometry and topology, but only the characteristic dimensions determining the pressure losses through the real rock fracture. Therefore, the total flow rate Q through the fracture can be written as:

$$Q(\nabla P) = \sum_{i=1}^{Z} w_i q(\nabla P, h_i) \tag{2}$$

Where $\nabla P = \Delta P/L$ is the absolute value of the pressure gradient, ΔP is the absolute value of the pressure drop between the inlet and the outlet of the fracture, L is the length of the straight channels, h_i are the different representative flow channel aperture classes and w_i is the width of each flow channel. In the preceding equation, the (w_i, h_i) data correspond to the flow channel Hydraulic Aperture Distribution (HAD) of the investigated rough-walled fracture, and $q(\nabla P, h_i)$ is the individual flow rate per unit width in a rectangular channel of aperture h_i, under a pressure gradient ∇P.

In the case of creeping one-dimensional flow of a Newtonian fluid of shear viscosity μ, $q(\Delta P, h_i)$ is given by Hele-Shaw's equation:

$$q(\nabla P, h_i) = \frac{h_i^3}{12\mu} \frac{\nabla P}{T} \tag{3}$$

with T being the hydraulic tortuosity and ∇P being the magnitude of the pressure gradient in the flow direction. Based on the results of previous experiments (Shojaei et al., 2019) which reported low tortuosity of the streamlines during the flow of yield stress fluids in a typical rock fracture, the rectangular flow channels were considered to be perfectly straight in the present model (T=1). Whereas h_i is known to be equal to the hydraulic aperture for Newtonian fluids, this equivalency is still to be proved in the case of yield stress fluids. Proving such equivalency will be the scope of the numerical simulations presented in Section 3 of the present manuscript.

For a Herschel Bulkley fluid, the $q(\nabla P, h_i)$ relationships are given by (Skelland, 1967; Chhabra and Richardson, 2008, Ferrás et al., 2012):

$$q(\nabla P, h_i) = \begin{cases} 2\left[\frac{n}{n+1}\left(\frac{\nabla P}{k}\right)^{1/n}\left[\frac{h_i h}{2}\left(\frac{h_i}{2} - \frac{h_0}{2}\right)^{1+1/n} - \frac{n\left(\frac{h_i}{2} - \frac{h_0}{2}\right)^{2+\frac{1}{n}}}{1+2n}\right]\right] & \text{for} \quad h_i \geq h_0 \\ 0 & \text{for} \quad h_i \leq h_0 \end{cases} \tag{4}$$

with $h_0 = 2\tau_0/\nabla P$ being the threshold aperture, which represent the aperture of a flow channel below which no flow occurs under the considered pressure gradient. Obviously, for $\tau_0 = 0$, n = 1 and k = μ, Eq. (4) becomes identical to Eq. (3).

2.2. Computation of aperture distribution by using YSM

The details of the algorithm used to compute the PSD of a porous sample from the raw flow rate vs. pressure gradient data $(Q_i, \nabla P_i)$ collected during injection of a yield stress fluid were provided by Rodríguez de Castro et al. (2014; 2016; 2018). Hence, only the essential features of the method and the procedure used to extend YSM to the case of rough-walled fractures are presented in this section.

In order to characterize the Hydraulic Aperture Distribution of a rough-walled rock fracture with YSM, an experiment must be performed that allows the collection of a set of $(Q_i, \nabla P_i)$ data, with Q_i being the total flow rate through the fracture. These steady-state measurements are performed during the injection of a Herschel-Bulkley fluid through the investigated fracture. The number of collected data couples is Z+1 (i = 1, ..., Z+1). From the Z+1 measurements, a set of Z representative flow channel apertures are defined as:

$$h_j = \alpha \frac{2\tau_0}{\nabla P_j} \quad (j = 1, \ldots, Z) \tag{5}$$
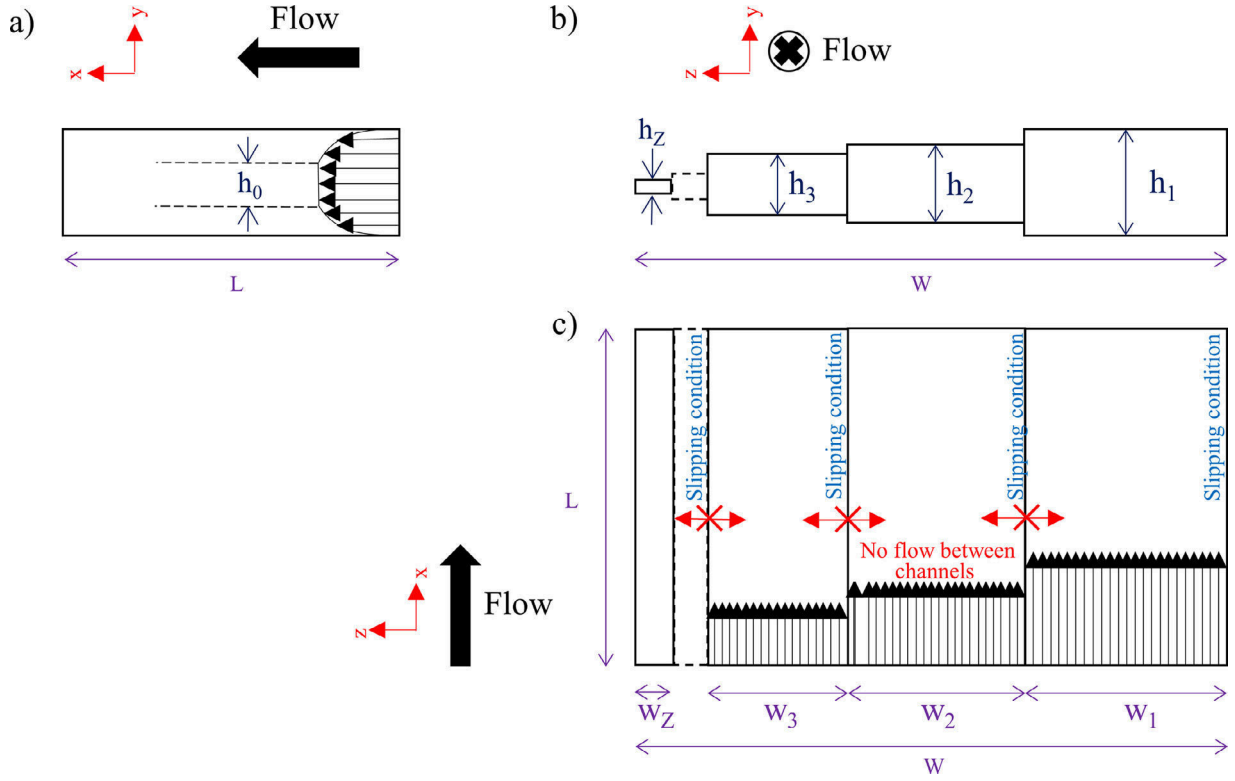
Fig. 1. Schematic representation of the bundle-of-rectangular-flow channels model: a) view of the vertical plane parallel to the main flow direction, b) view of the cross-section perpendicular to flow direction displaying the different apertures of the rectangular flow channels ($h_1 \ldots h_Z$) and c) view of the horizontal plane parallel to the main flow direction displaying the different widths of the rectangular flow channels ($w_1 \ldots w_Z$). Black arrows in a) and c) schematically represent the velocity profiles of the yield stress fluid in each flow channel. The aperture class h_Z is considered to be smaller than $h_0 = 2\tau_0/\nabla P$, which results in no flow occurring in the channel of aperture h_Z.

It must be taken into account that flow under a given pressure gradient ∇P_j only occurs in channels with an aperture strictly larger than $\frac{2\tau_0}{\nabla P_j}$. Consequently, the value of the numerical factor α in Eq. (5) must be greater than unity. A full description of the procedure followed to compute the value of α was presented in the literature (Rodríguez de Castro et al., 2014) and is adapted to the case of fractures in the present section.

With the objective of extending YSM method to rough-walled rock fractures, it is first assumed that the bundle of Z straight parallel flow channels with rectangular cross-sectional areas presented in Subsection 2.1 is capable of accurately predicting the relationship between flow rate and generated pressure losses. Then, the width w_j of the flow channel with aperture h_j is calculated as being the maximum positive value of w_j for which the following condition is respected:

$$Q_s \geq \sum_{g=1}^{j} w_g q(\nabla P_s, h_g) \quad \text{for} \quad s \geq j + 1 \tag{6}$$

where $q(\nabla P_s, h_g)$ is given by Eq. (4). The width, w_1, of the flow channel with the largest aperture h_1 is first determined by solving the system of inequations (6) for $s \geq 2$, then w_2 was calculated for $s \geq 3$ and then the width of the flow channels of smaller and smaller aperture are computed until w_Z (the width of the flow channel with the smallest aperture) is calculated. At the end of this process, a set of (h_j, w_j) data is obtained. From these results, the relative frequency $p(h_j)$ of each flow channel aperture class h_j is given by:

$$p(h_j) = \frac{h_j w_j}{\sum_{i=1}^{Z} h_i w_i} \tag{7}$$

The suitable value of α, named $\alpha*$, is calculated as follows: first, $\alpha = 1$ is used to calculate the (h_j, w_j) data , and the total width of the flow channels $\sum_{i=1}^{Z} w_i$ is computed. Then, the same procedure is repeated by successively increasing the value of α with a scanning step of δ ($\delta = 0.1$ was used in the present work) until the (h_j, w_j) data corresponding to $\alpha = 2$ has been calculated. $\alpha*$ is selected as being the value of α that minimizes the absolute value of the difference between the actual width of the fracture W and the calculated one, i.e., $|W - \sum_{i=1}^{Z} w_i|$. From the computed (h_j, w_j) data, the calculated macroscopic relationship between the total flow rate through the fracture Q and the pressure gradient ∇P can be obtained using Eq. (2). It must be borne in mind that flow channels with large apertures contribute more significantly to the total flow rate. Hence, the scanning procedure to calculate each w_j, should be more refined when the considered aperture is large. For this reason, the step used in the scanning procedure (different from δ) is defined as: $\text{Step}_j = \zeta q(\nabla P_{Z+1}, h_Z)/q(\nabla P_{Z+1}, h_j)$, where ζ is a coefficient that quantifies the refinement of scanning. $\zeta = 0.05 \times W$ was used in the considered experiments.

3. Numerical simulation of the flow of yield stress fluids through 2D rough-walled rock fractures

A set of 2D numerical simulations were performed in order to gain further insight into the physical meaning of the HAD provided by YSM in the case of rough-walled rock fractures. A key objective was to identify the regions of the fracture where most pressure drops were generated during the injection of yield stress fluids and their correlation with the hydraulic aperture as determined for Newtonian fluids.
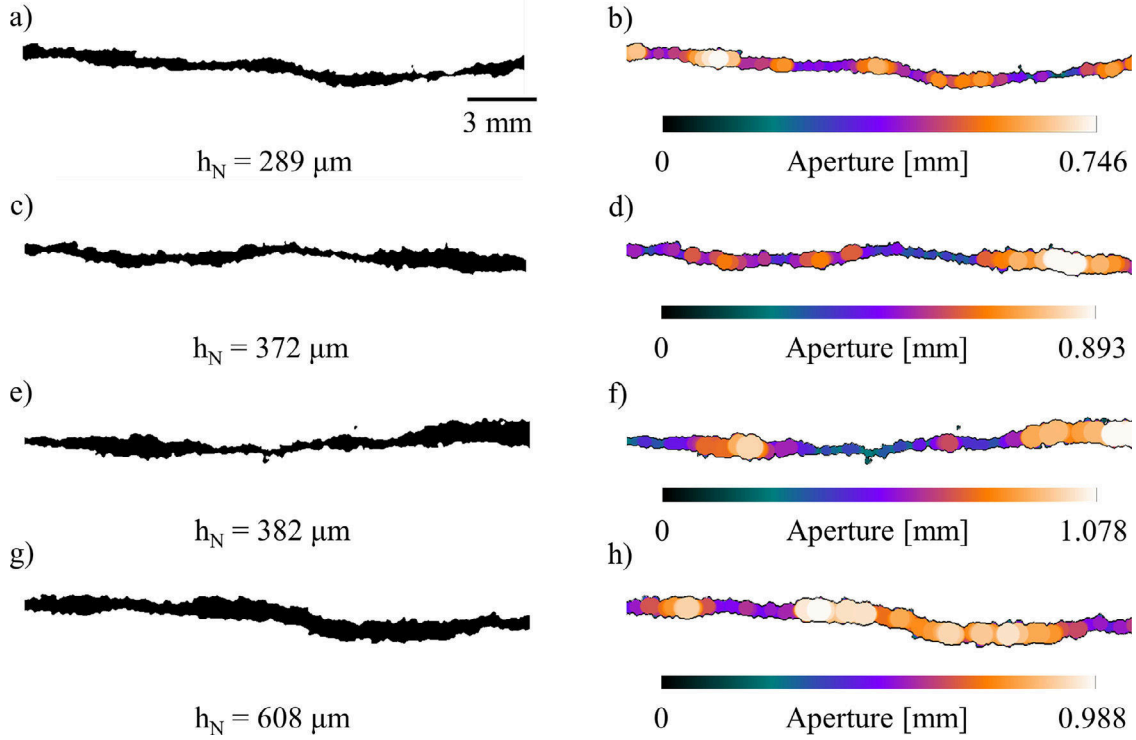
a)

3 mm

$h_N = 289 \ \mu m$

b)

0   Aperture [mm]   0.746

c)

$h_N = 372 \ \mu m$

d)

0   Aperture [mm]   0.893

e)

$h_N = 382 \ \mu m$

f)

0   Aperture [mm]   1.078

g)

$h_N = 608 \ \mu m$

h)

0   Aperture [mm]   0.988

Fig. 2. Subset of 2D slices obtained from the freely available X-ray microtomography results of the Berea sandstone fracture obtained by Karpyn et al. (2016) and investigated in the current numerical simulations. The Newtonian hydraulic apertures of these slices are (a-b) 289 μm, (c-d) 372 μm, (e-f) 382 μm, and (g-h) 608 μm. The segmented slices are presented in the left part of the Fig., while the aperture map is represented in the right part.

3.1. Investigated media

Karpyn et al. (2007) conducted X-ray microtomography experiments in order to map the internal structure of an artificially induced rough fracture in a Berea sandstone, which was oriented parallel to the natural bedding of the rock. The results of such X-ray microtomography experiments are freely available (Karpyn et al., 2016). From the reconstructed fracture geometry, the four segmented 2D slices displayed in Fig. 2 were used in the present work as an input to the numerical simulations. Moreover, the BoneJ algorithm (Doube et al., 2010) included in the open source image-processing software ImageJ (Schindelin et al., 2012) was used to determine the local aperture map of the 2D slices. Then, a first set of Newtonian direct numerical simulations was performed to determine the Newtonian hydraulic aperture h_N of these 2D slices. The h_N values are also given in Fig. 2. It can be seen that all the 2D slices present a wide range of local apertures, and the value of h_N is strongly affected by the presence of narrow constrictions, as expected from the important pressure losses produced in these regions.

3.2. The procedure for numerical experiments

Numerical simulations are commonly used to study the characteristics of flow systems whose mathematical models are too tedious to provide analytical solutions, as it is the case of the flow of yield stress fluids through real rough-walled fractures (Hewitt et al., 2016; Chaparian and Tamiasola, 2020). Full 3D CFD simulations of this type of flows can become prohibitively expensive in terms of computational resources, given that the two in-plane dimensions of the fracture are much larger than the fracture aperture. In order to avoid the computational cost of a fully 3D approach, Morris et al. (2015) developed a simulator for the flow of power-law, Bingham and Herschel-Bulkley fluids through fractures by introducing a 2D aperture-averaged analytic solution and compared the results to those obtained for a 3D model implemented in a commercial code. These authors showed that the 2-D model was capable of

predicting the location of the fluids in non-mixing flows. Also, for the first time, Zhang et al. (2019) carried out 3D numerical simulations of the flow of shear-thinning fluids without yield stress through a rough-walled rock fracture, by extracting the input geometry from a computed microtomography image.

Recently, Rodríguez de Castro and Agnaou (2019) and Rodríguez de Castro et al. (2020) performed numerical simulations that provided the velocity and viscosity maps for a Herschel-Bulkley fluid flowing in a set of 2D porous media. These media consisted of real and idealized packings of particles of various shapes and sizes. Following the procedure described in these previous works, the finite element-based numerical simulation software COMSOL Multiphysics version 5.3. (2017) was used in the present study to solve the flow problems under interest. Analogously to the work of Bauer et al., (2019), Stokes flow was considered in the numerical simulations and the following equations were solved:

$$0 = \nabla \cdot \mathbf{\Pi} - \nabla P$$

with $\mathbf{\Pi}$ being thethe deviatoric stress tensor and P being the pressure. For a Herschel-Bulkley fluid, $\mathbf{\Pi}$ can be written as follows:

$$\mathbf{\Pi}_{i,j} = 2\mu \Delta_{i,j}$$

where Δ is the strain rate tensor, i.e., $\Delta_{i,j} = \frac{1}{2}\left(\frac{\partial u_i}{\partial x_j} + \frac{\partial u_j}{\partial x_i}\right)$ with $\mathbf{u}$ being the velocity vector and (x_i, x_j) being the spatial coordinates. A generalized shear rate $\dot{\gamma}$ can be defined by using Einstein's summation convention: $\dot{\gamma} = \sqrt{2\Delta_{i,j}\Delta_{i,j}}$. The following model was implemented to quantify the local viscosity of the yield stress fluid:

$$\mu = \min\left[\mu_{max}, \left(k\dot{\gamma}^{n-1} + \frac{\tau_0}{\dot{\gamma}}\right)\right]$$

where μ_{max} corresponds to a maximum viscosity. The Herschel-Bulkley shear-rheology parameters of the investigated fluid were $\tau_0 = 10$ Pa, $k = 1$ Pa s^n and $n = 0.5$. A value $\mu_{max} = 10000$ Pa s was selected as a compromise between numerical stability and accuracy. Indeed, using extremely high μ_{max} values results in large viscosity gradients within the

computational domain and instabilities. On the other hand, low μ_{max} values fail to emulate a yield stress. The chosen value of μ_{max} corresponds to shear rates lower than $\dot{\gamma} = 10^{-3} \text{s}^{-1}$. Further details on the viscosity regularisation methods for visco-plastic fluid flow computation were provided in the literature (Frigaard and Nouar, 2005).

The computational domain, which is a 2D section of a fracture as shown in Fig. 2, was discretized using unstructured meshes composed of triangular element faces. The elementary control volumes are defined around each node joining the centres of mesh elements. The values obtained at mesh nodes are interpolated based on a linear Lagrangian interpolation for the pressure whereas a quadratic interpolation is adopted for the velocity components. The *Creeping Flow* module, designed for solving Stokes flows was used. For each 2D geometry, various inlet pressures were imposed as boundary conditions while keeping the outlet pressure equal to 0, and the corresponding steady-state total flow rates per unit width (m²/s) were computed. The non-linear system of equations was solved using the *COMSOL Stationary Solver*. The solution is sought by making use of a Newton-Raphson algorithm that starts with the initial conditions as an initial guess. The solution is considered converged upon reaching a residual below a relative tolerance of 10^{-3}. Within each Newton-Raphson iteration, the resulting system of linearized equations is solved using the direct solver PARDISO (Schenk 2004). Simulations are initiated with the fluid at rest. To go further, the influence of the chosen μ_{max} value was also evaluated by comparing the results obtained by using the original $\mu_{max} = 10000$ Pa s value and a ten times greater $\mu_{max} = 100000$ Pa s value in the case of the 2D geometry with hydraulic aperture $h_N = 372$ μm and imposing an inlet pressure of 3000 Pa (the smallest one under consideration). The observed differences in terms of both the average shear rate and the total flow rate per unit width (used in YSM algorithm) were negligible (1.20% and 2.2%, respectively).

As reported by Lavrov (2013a), it is sometimes advantageous to replace a real rough-walled fracture with an "equivalent" fracture with parallel smooth walls when incorporating fluid flow through fractures into higher-level models such as reservoir simulators. In this regard, the equivalent aperture h_{eq} (di Federico, 1997; 1998) is defined as the aperture of a fracture with parallel smooth walls that would exhibit the same flow rate under a given applied pressure gradient as the real rough-walled rock fracture. In the case of Newtonian flow, $h_{eq} = h_N$ for any considered pressure gradient. Tsang (1992) discussed the differences between the numerous definitions and notations of fracture apertures, showing that the hydraulic aperture and the aperture obtained from tracer tests should not be assimilated. In this respect, tracer tests were performed by Nowamooz et al. (2013) in the same two fractures that will be investigated in the current work. The distribution of local permeabilities were computed from the results of the tracer tests assuming a stratified medium model, which required image-processing stages and calibration. Regarding the determination of the hydraulic apertures of rock fractures, borehole pumping tests were used by other authors for this purpose (Barton et al., 1985), as listed in Table 1. Also, Cao et al. (2016) stated that knowledge of the Hydraulic Aperture Distribution (HAD) of a fracture is urgently needed in engineering construction and analytical models at the engineering field scale. In the same work, the authors presented a method for the measurement of HAD based on "*in situ*" camera measurements combined with borehole water-pressure tests, and discussed the relationships between hydraulic aperture and mechanical aperture.

From Eq. (4), the following expression can be written to calculate the equivalent apertures h_{eq} of the 2D considered flow channels from the numerically computed (q_j, ∇P_j) data for each imposed value of ∇P_j:

$$q_j\left(\nabla P_j, h_{eq}\right) = \begin{cases} 2\left[\frac{n}{n+1}\left(\frac{\nabla P_j}{k}\right)^{1/n}\left[\frac{h_{eq}}{2}\left(\frac{h_{eq}}{2}-\frac{h_0}{2}\right)^{1+1/n} - \frac{n\left(\frac{h_{eq}}{2}-\frac{h_0}{2}\right)^{2+\frac{1}{n}}}{1+2n}\right]\right] & \text{for } h_{eq} \geq h_0 \\ 0 & \text{for } h_{eq} \leq h_0 \end{cases}$$

(8)

Eq. (8) can be numerically solved to obtain h_{eq}. For example, this was achieved by using the differential evolution method in the present work. It is noted that, in contrast to the constant value of h_N, h_{eq} cannot be safely assumed to be constant for different values of ∇P_j in the case of yield stress fluids, given the non-linear relationship between flow rate and pressure gradient.

According to Eq. (2) the relationship $Wq(\nabla P, h_N) = \sum_{i=1}^{Z}(w_i q(\nabla P, h_{N,i}))$ can be expressed as $W \frac{h_N^3}{12\mu} \frac{\nabla P}{T} = \sum_{i=1}^{Z}(w_i \frac{h_{N,i}^3}{12\mu} \frac{\nabla P}{T})$ for the injection of a Newtonian fluid, so $Wh_N^3 = \sum_{i=1}^{Z}(w_i h_{N,i}^3)$ with $W = \sum_{i=1}^{Z} w_i$ and $h_{N,i}$ being the Newtonian hydraulic aperture of each flow channel. Given that yield stress fluids are used in YSM, the question that arises is whether $h_{N,i}$ is still representative of the characteristic aperture that should be used in the bundle model so as to accurately predict the relationship between flow rate and pressure loss. In other words: is $\sum_{i=1}^{Z}(w_i q(\nabla P, h_{N,i}))$ still equivalent to the total flow rate $Wq(\nabla P, h_{eq})$ through a rough-walled fracture for the injection of a Herschel-Bulkley fluid? To answer this question, it will be first considered that each 2D fracture used in the present numerical experiments can be assimilated to an individual flow channel traversed by the yield stress fluid during its flow through a real fracture, providing a representation of the evolving aperture of such flow channel throughout the medium. Then, the equivalent aperture h_{eq} of a constant-section flow channel providing the same pressure loss-flow rate relationship as the actual 2D geometries presented in Fig. 2 for a wide range of flow rates will be computed from the results of the numerical experiments with Herschel-Bulkley fluids. Finally, the values of h_{eq} computed for the 2D geometries will be compared to the corresponding values of h_N to assess the closeness of both quantities. It should be highlighted that the objective of the current numerical simulations is not to assimilate the microscopic mechanisms arising during the flow of yield stress fluids through real 3D fractures to the mechanisms arising in a 2D geometry. Indeed, significant differences exist between the 2D and the 3D cases. In particular, a preferential flow channel with higher flow rate than the one produced in the constrictions can be formed in 3D rough-walled rock fractures. In contrast, the highest flow velocities are located in the constricted zones in the case of 2D channels, as will be shown in Subsection 5.1.

4. Experimental: flow of Yield Stress fluids through rough-walled rock fractures

Rodríguez de Castro and Radilla (2017) carried out flow rate vs. pressure gradient measurements during the injection of a yield stress fluid through two well-characterized rough-walled rock fractures. In this section, the full experimental data set obtained by these authors is used as an input to the YSM algorithm to compute the HAD of both fractures.

4.1. Investigated media

Experimental works dealing with the injection of yield stress fluids in rough-walled fractures are scarce (Rodríguez de Castro and Radilla, 2017; Shojaei et al., 2019). Rodríguez de Castro and Radilla (2017) conducted a set of laboratory experiments in which a concentrated polymer solution exhibiting a yield stress was injected through two transparent epoxy resin replicas of a granite fracture and a Vosges sandstone fracture. The details of the procedure followed for the fabrication of these fracture replicas are available elsewhere (Isakov et al., 2001; Nowamooz et al., 2013). The width W, total length, permeability K, Newtonian hydraulic aperture h_N and mechanical aperture (arithmetic average) h_m of both fractures are listed in Table 2. The aperture maps were previously obtained by Nowamooz et al. (2013) by means of an image processing procedure based on the attenuation of a light source following the law of Beer-Lambert, and are displayed in Fig. 3.

Table 2
Width W, total length, permeability K, Newtonian hydraulic aperture h_N, mechanical aperture h_m and number of experimental data Z +1 for the experiments with the two rough-walled rock fractures. The values of h_m were obtained from Nowamooz et al. (2013).

Fracture	W[cm]	Total length[cm]	$K[m^2]$	h_N[m]	h_m[m]	Z +1[–]
Granite	15.5	33	6.1×10^{-8}	8.5×10^{-4}	9.00×10^{-4}	45
Vosges sandstone	14.8	26	2.1×10^{-8}	5.0×10^{-4}	8.47×10^{-4}	45

a)

b)

h (mm)

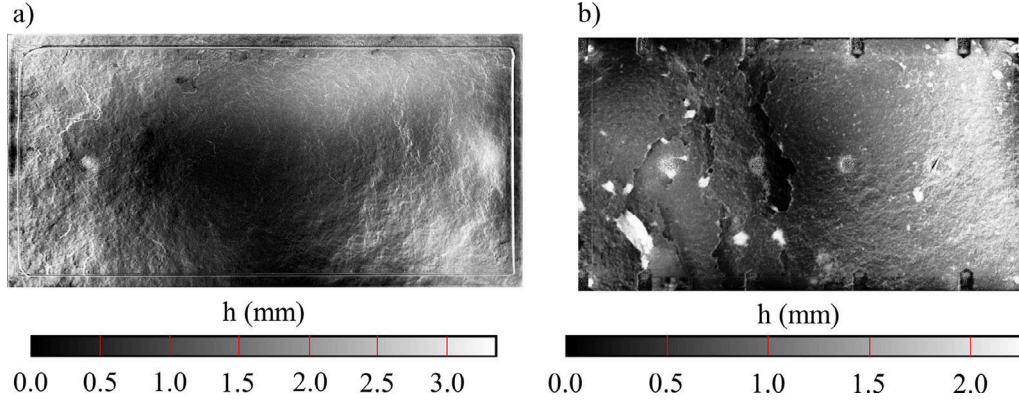0.0 0.5 1.0 1.5 2.0 2.5 3.0

h (mm)

0.0 0.5 1.0 1.5 2.0

Fig. 3. Aperture maps of the two investigated fractures (data obtained from Nowamooz et al., 2013): (a) granite fracture and (b) Vosges sandstone fracture. In these aperture maps, darker colours correspond to smaller apertures.

For both fractures, the smallest apertures are located in the central part and the largest apertures are located near the inlet and the outlet. Moreover, the apertures of the Vosges sandstone fracture are more variable at the lower half than at the upper half, while the spatial variability appears to be relatively high across the entire granite fracture area.

As showed in the work of Nowamooz et al. (2013), the constrictions in the central part of these fractures constituted a barrier to fluid flow, especially in the case of shear-thinning and yield stress fluids, as the pressure loss sensitivity to aperture is higher than for a Newtonian one (Roustaei et al., 2016). On this subject, Shojaei et al. (2019) experimentally determined the velocity map of a yield stress fluid flowing through the same Vosges sandstone fracture, and characterized the apparent shear rheology of the fluid. The characterization of the velocity map was achieved by performing a Particle Image Velocimetry (PIV) analysis on a set of images obtained during the flow of a pre-generated foam exhibiting a yield stress through the transparent replica, in order to monitor the position of the bubbles at different times. The authors showed that the aperture variation strongly affects the apparent viscosity of the foam and the velocity contrast between preferential flow channels and stagnant zones.

4.2. Experimental setup and fluid properties

The signature of HAD in the flow rate vs pressure gradient curve is only present at low flow rates for which the fluid remains unyielded in a fragment of the fracture, i.e., in some of the flow channels depending on the applied pressure gradient. Given that this signature needs to be present in the Q vs. ∇P data used as input to YSM algorithm, the particularly wide range of flow rates (∼ 3.6 orders of magnitude) imposed in the experiments of Rodríguez de Castro and Radilla (2017) is suitable for its use in YSM algorithm. The experimental setup and procedure presented in the following lines corresponds to the one used by these authors.

The calibration of the yield stress fluid was discussed in previous works (Rodríguez de Castro et al, 2018). Xanthan gum aqueous solutions were selected, due not only to their low degree of viscoelasticity and their negligible thixotropic behaviour, but also to their environmentally friendly nature. The Herschel-Bulkley parameters of injected fluid were $\tau_0 = 7.36$ Pa, k = 0.365 Pa s^n and n = 0.52. The shear rheology of

the xanthan solutions used in the present experiments was characterized by means of a stress-controlled rheometer equipped with a cone-plate geometry. All rheological measurements were performed at 20°C by applying shear stresses linearly sampled from 0 to a maximum value producing a shear rate of approximately 1000 s^{-1}. The $(\tau_j, \dot{\gamma}_j)$ experimental data (presented by Rodríguez de Castro and Radilla, 2017) were fitted to a Herschel-Bulkley law by minimizing the sum:

$$\sum_{j=1}^{N} \left[\left(\tau_0 + k\dot{\gamma}_j^n \right) - \tau_j \right]^2 \dot{\gamma}_j$$

with N being the number of $(\tau_j, \dot{\gamma}_j)$ data. By doing so, the values of the yield stress τ_0, the power-law index n, and the consistency k were determined. The square of the difference between τ_j and $(\tau_0 + k\dot{\gamma}_j^n)$ was weighted by $\dot{\gamma}_j$, following the procedure presented by Rodríguez de Castro et al. (2014). Moreover, a set of effluent fluid samples were collected at the outlet of the fractures after injection at the highest flow rate. The effluent rheograms were determined and compared to that of the inflowing fluid in order to assess polymer degradation, retention of the polymer on the fracture walls and the constancy of the rheological parameters during all the experiments. No significant difference was observed between the rheograms, so polymer degradation and polymer retention were proved to be negligible. The results also showed that the variation in the values of the Herschel-Bulkley parameters over the set of experiments was not significant

Two different experimental setups were used depending on the injection flow rates. For the low and moderate flow rates, ranging from 1.67×10^{-8} to 1.67×10^{-6} m^3/s, an open injection circuit was used in which the aqueous polymer solution was injected through the fracture at a flow rate imposed by a dual piston pump. For the highest flow rates, ranging from 2.50×10^{-6} to 6.94×10^{-5} m^3/s, the circuit was closed. In this second configuration, a volumetric pump was used to inject the yield stress fluid from a tank situated upstream of the rough-walled rock fracture, and the fluid was continuously recirculated to the tank from the outlet of the fracture. Also, a positive displacement flow meter was installed at the outlet of the volumetric pump to measure the injection flow rate. In both configurations, the pressure drop was measured with a differential pressure sensor over a distance of L = 20.5 cm for the Vosges sandstone fracture and L = 27 cm for the granite fracture. The range of

the pressure sensor was adjusted by installing different membranes from 0–1400 Pa to 0–56,000 Pa with an accuracy of $\pm 0.3\%$ of the full scale. The range of the piston pump was from 1.67×10^{-9} to 1.67×10^{-6} m^3/s with an accuracy of 2% while the range of the flow meter installed at the outlet of the volumetric pump was from 1.94×10^{-6} to 1.38×10^{-4} m^3/s with an accuracy of 1%.

4.3. Experimental procedure

Both rough-walled fractures were saturated with CO_2 (more water-miscible gas than air) prior to saturation with the yield stress fluid to avoid the formation of gas bubbles during the measurements. Then, the fractures were fully saturated with the yield stress fluid, which was subsequently injected at 45 different flow rates ranging from 1.67×10^{-9} to 4.72×10^{-5} m^3/s through the granite fracture, and at 38 flow rates that lie between 3.33×10^{-9} m^3/s and 2.78×10^{-5} m^3/s through the Vosges sandstone fracture. In each series, the flow rate was steeply increased and the corresponding steady-state pressure drop was measured. Each measurement was repeated four times and the uncertainty related to the repeatability was calculated as $\pm 2\sigma$, with σ being an estimate of the relative standard deviation of the measurements (95% confidence interval). All experiments were performed at T = 20±1 °C.

It is highlighted that the minimum number of experiments required to obtain an hydraulic aperture distribution with an acceptable level of accuracy in YSM depends on the statistical dispersion of the microstructural dimensions of the characterized sample (more dispersed samples require more measurements). This statistical dispersion is unknown *a priori* unless some microstructural information is known beforehand. This issue also arises in the case of other porosimetry methods, such as MIP and X-ray microtomography techniques. In particular, the choice of minimum resolution in a microtomography measurement is often challenging. Nevertheless, for the case of YSM experiments, some general guidelines and recommendations can be made:

- It should be ensured that the maximum flow rate imposed during the experiments Q_{max} is adequate to make the yield stress fluid flow through all the channels of the rough-walled fracture. As explained in Subsection 5.3., the preceding condition is respected if the fit of the data points at the highest flow rates leads to a power law of ∇P with an exponent of $1/n$.
- The minimum flow rate imposed during the experiments Q_{min}, should be as low as possible, and is given in practice by the technical limitations of the experimental setup. However, it must be checked that the value $\frac{2\tau_0}{\nabla P_{min}}$ is close to the largest hydraulic aperture sizes expected in the characterized fracture.
- Rodríguez de Castro (2014) tested different sampling procedures for YSM in order to evaluate their suitability. Based on the results reported in this previous work, it is recommended that, during each experiment, a set of different flow rates Q_j (j = 1...Z + 1) should be imposed to the injected the yield stress fluid, following the sequence below:

$$Q_j = Q_{min} \left(\frac{Q_{max}}{Q_{min}} \right)^{\left(\frac{Z+1-i}{Z} \right)}$$

- Based on the previous experimental and numerical works listed in Table S1 of the supplementary material, in which YSM was used to characterize high and moderate permeability samples, it is recommended that the number of experimental data Z + 1 should be greater than 30. However, the accuracy of the obtained HAD is expected to be improved by increasing the number of measurements.

5. Results

5.1. Numerical results: velocity and viscosity maps

Some examples of the velocity maps obtained by performing the numerical simulations presented in Subsection 3.2 are presented in Fig. 4,

showing the existence of a wide range of velocities within a single 2D channel, with much higher velocity values in the constrictions of the fracture and lower velocity values in the vicinity of the walls, as expected. It is highlighted that the extension of the high-velocity regions (warmer colours in Fig. 4) is greater for the 2D flow channels of greater hydraulic apertures.

Mitsoulis and Huilgol (2004) numerically investigated the flow of Bingham fluids through conduits with an abrupt expansion. Their results showed that the plug region of unyielded fluid breaks at the location of the drastic aperture change resulting in the formation of blobs of unyielded material in the corners of the expansion. The size of such blobs increases by decreasing the injection flow rates (as Bingham number increases). De Souza Mendes et al. (2007) also showed that unyielded regions appear first in the corners of an abrupt expansion, whereas for the smooth geometries of Roustaei and Frigaard (2013), unyielded fluid was first observed in the deepest part of the channel, i.e., with the highest aperture. The viscosity maps computed from the numerical experiments performed in the 2D fracture with h_N = 372 μm are presented in Fig. 5 for different values of the imposed pressure drop. This 2D fracture presents important aperture variations, with a central constricted area. Fig. 5 shows that the plug breaks close to the constriction, in the low local aperture zones, forming islands of unyielded fluid. Also, the fluid remains unyielded in the corners of the sections with large local apertures.

Roustaei et al. (2016) analysed the so-called "fouling layers" generated at the walls of smooth 2D channels during the flow of a yield stress fluid, in which residual fluid is held stationary. This geometric effect had also been observed in various experimental and computational/analytical studies (e.g., Mitsoulis and Huilgol, 2004, de Souza Mendes et al., 2007; Chevalier et al., 2013, Roustaei and Frigaard, 2013). Moreover, Frigaard and Ryan (2004) analytically showed that in a conduit with regularly and smoothly varying aperture, an intact and continuous plug exists throughout the channel. However, as the roughness of the walls increases, the plug breaks, creating three distinct regions: the shear flow near the walls, the stagnant zones forming a group of unconnected blobs and the regions of extensional flow between the islands of unyielded material. Based on the preceding observations, Roustaei et al. (2016) suggested that the size of the flowing region (without including the fouling layer in which the fluid remains stagnant) governs pressure losses during the flow of a yield stress fluid, rather than the aperture of the fracture. Nevertheless, as stated by Lavrov (2013a), little is known about the features of the flow field for a yield-stress fluid flowing in a realistic rough-walled fracture.

In the present work, the aperture variation over a given fracture was considered to be smooth when the minimum-to-maximum aperture ratio was higher than 0.4 (arbitrary value). In an attempt to elucidate the unyielding behaviour of a yield stress fluid in a realistic 2D fracture with smooth aperture variation, the viscosity maps obtained at low pressure gradients were computed from an additional set of numerical experiment performed in the fracture with h_N = 608 μm (minimum-to-maximum aperture ratio of 0.43). These experiments were performed following the procedure described in Section 3. The results are presented in Fig. 6, confirming the existence of unconnected blobs of unyielded material inside the rough fracture with smoothly changing aperture. Also, the thickness of the fouling layer generated in the vicinity of the walls decreases when the applied pressure gradient is increased.

5.2. Numerical results: h_{eq} calculation

Four sets of (q_i, ∇P_i) data were computed for the flow through the 2D channels of variable aperture by using the procedure presented in Subsection 3.1, and the results are displayed in Table 3. As explained in Subsection 3.2, the aperture h_{eq} of an equivalent fracture with parallel smooth walls exhibiting the same flow rate under a given applied pressure gradient as the real rough-walled flow channel was calculated for the geometries presented in Fig. 2. This was achieved by solving
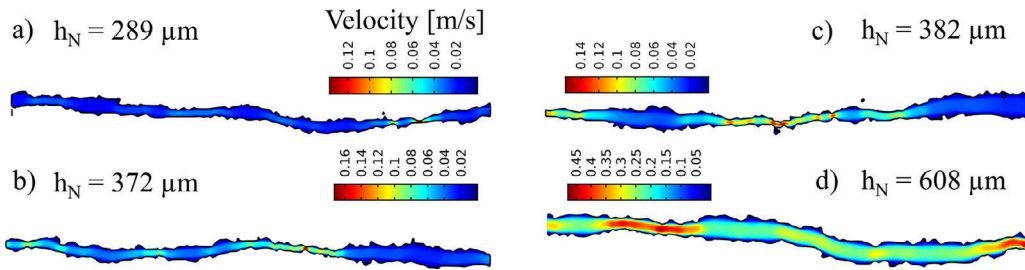
Fig. 4. Velocity magnitude maps as determined by the numerical simulations performed in the present work for the injection of the yield stress fluid through 2D channels of different Newtonian hydraulic apertures The imposed pressure drop was 5000 Pa in all cases.
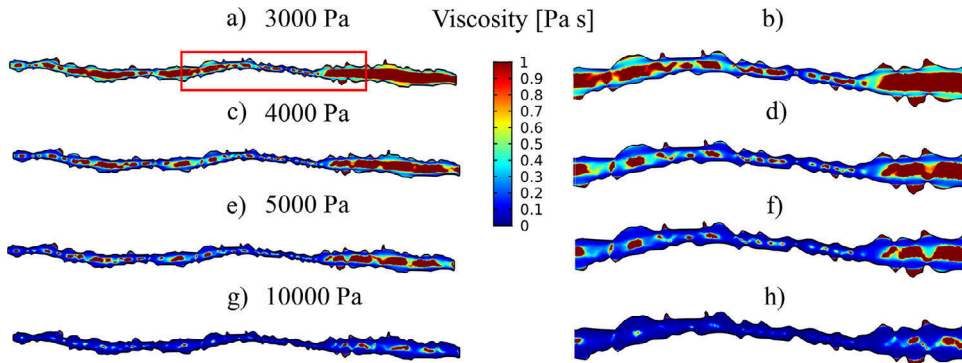

Fig. 5. Shear viscosity maps obtained by the numerical simulations for the injection of the same yield stress fluid through a 2D flow channel of Newtonian hydraulic aperture $h_N = 372$ μm under different values of the imposed pressure drop: (a,b) 3000 Pa, (c,d) 4000 Pa, (e,f) 5000 Pa, (g,h) 10000 Pa. (a), (c), (e), (g) display the viscosity map in the whole fracture, while (b), (d), (f), (h) display enlarged images of the region of the fracture contained within the red rectangle represented in (a). Dark red regions correspond to the zones in which the shear viscosity values are greater than 1 Pa s, and are assimilated to islands of unyielded plug.
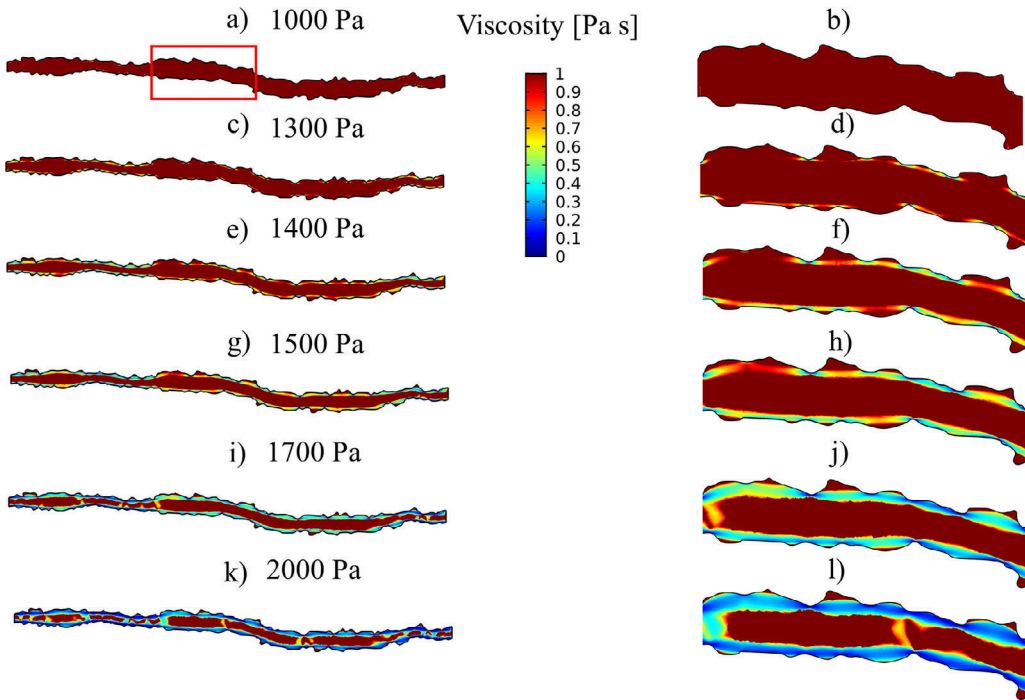
Fig. 6. Shear viscosity maps obtained by the numerical simulations performed in the present work for the injection of the same yield stress fluid through a fracture of Newtonian hydraulic aperture $h_N = 608$ μm under different pressure drops: (a,b) 1000 Pa, (c,d) 1300 Pa, (e,f) 1400 Pa, (g,h) 1500 Pa, (i,j) 1700 Pa and (k,l) 2000 Pa. (a), (c), (e), (g), (i) and (k) display the viscosity map in the whole fracture, while (b), (d), (f), (h), (j) and (l) display enlarged images of the region of the fracture contained within the red rectangle represented in (a). Dark red regions correspond to the zones in which the shear viscosity values are greater than 1 Pa s, and are assimilated to islands of unyielded plug.

Eq. (8) with the computed $(q_i, \nabla P_i)$ data as input. The variation of the calculated h_{eq} values when varying q_i was shown to be negligible within the investigated range of flow rates. The computed values of h_{eq} are listed in Table 4, together with the corresponding values of the Newtonian hydraulic aperture h_N. More details for the calculation of h_{eq} are provided as supplementary material (Figure S1).

From Table 4, it can be deduced that h_{eq} is very close to h_N in all the investigated realistic rough-walled 2D flow channels. These results are consistent with the numerical modelling of shear-thinning flows through rough-walled fractures performed by di Federico (1997) and Lavrov (2013). In particular, di Federico (1997) showed that, for the flow perpendicular to aperture variation, h_{eq} is only slightly higher than

Table 3
Range of(q_i, ∇P_i) computed data for the investigated flow channels with different Newtonian hydraulic apertures.

Channel 1:h_N = 289 μm		Channel 2:h_N = 372 μm		Channel 3:h_N = 382 μm		Channel 4:h_N = 608 μm	
∇P_i [Pa/m]	q_i [m²/s]	∇P_i [Pa/m]	q_i [m²/s]	∇P_i [Pa/m]	q_i [m²/s]	∇P_i [Pa/m]	q_i [m²/s]
1.82×10^5	4.48×10^{-6}	9.11×10^4	3.84×10^{-7}	9.11×10^4	6.59×10^{-7}	4.56×10^4	5.23×10^{-7}
2.28×10^5	9.06×10^{-6}	1.37×10^5	3.59×10^{-6}	2.28×10^5	2.25×10^{-5}	1.37×10^5	3.76×10^{-5}
4.56×10^5	5.63×10^{-5}	1.82×10^5	9.70×10^{-6}	4.56×10^5	1.29×10^{-4}	2.28×10^5	1.48×10^{-4}
9.11×10^5	2.73×10^{-4}	2.28×10^5	1.83×10^{-5}	9.11×10^5	6.04×10^{-4}	4.56×10^5	7.48×10^{-4}
1.37×10^6	6.52×10^{-4}	4.56×10^5	1.11×10^{-4}	1.37×10^6	1.44×10^{-3}	9.11×10^5	3.33×10^{-3}
1.82×10^6	1.19×10^{-3}	9.11×10^5	5.24×10^{-4}	1.82×10^6	2.59×10^{-3}	1.37×10^6	7.76×10^{-3}
2.28×10^6	1.90×10^{-3}	1.37×10^6	1.24×10^{-3}	2.28×10^6	4.11×10^{-3}	1.82×10^6	1.40×10^{-2}
		1.82×10^6	2.27×10^{-3}			2.28×10^6	2.22×10^{-2}
		2.28×10^6	3.61×10^{-3}				

Table 4
Newtonian hydraulic apertures h_N and equivalent apertures for yield stress fluid flow h_{eq} of the rough-walled channels investigated in the numerical experiments.

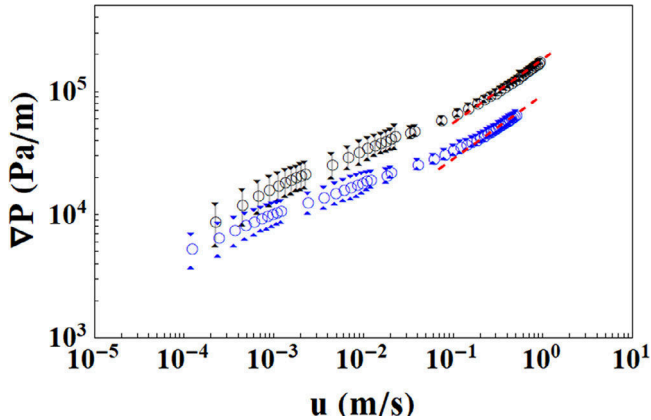| Rough-walled 2D channel	h_N [μm]	h_{eq} [μm]
Channel 1	289	335
Channel 2	372	381
Channel 3	382	401
Channel 4	608	623

Fig. 7. Raw u-∇P measurements plots obtained from the YSM experiments (Rodríguez de Castro and Radilla, 2017). These data points are used as input to the algorithm allowing the determination of AD. Blue symbols correspond to the granite fracture and black symbols correspond to the Vosges sandstone fracture. Red dashed lines represent a power law of ∇P with an exponent of 1/n fitted to the data points corresponding to the four highest flow rates for each case (as discussed in Subsection 5.3).

h_N for shear-thinning fluids (n < 1). This was also the case of realistic aperture distributions in which the aperture varies both in parallel and perpendicular directions to fluid flow, as the ones investigated in the laboratory experiments. As a consequence of these observations, the (w_i,h_i) data computed with YSM from the experimental (Q_i, ∇P_i) data by assuming the bundle of parallel rectangular flow channels presented in Subsection 2.1. are expected to be close to the distribution of Newtonian hydraulic apertures of the different flow channels.

5.3. Experimental results: ∇P vs Q measurements

The results of the pressure drop vs flow rate measurements provided by the YSM laboratory experiments presented in Section 4 are displayed in Fig. 7. It should be noted that the average velocity u = $Q/(h_N \times W)$ is represented in the horizontal axis of this figure instead of the flow rate in order to facilitate comparison between the two fractures. Careful

observation of the experimental data shows that higher pressure gradients are generated in the Vosges sandstone fracture as compared to the granite fracture for a given value of average velocity in the region u ≥ 10^{-4} m/s. This is consistent with the lower Newtonian hydraulic aperture value of the Vosges sandstone reported in Table 2. However, the measured pressure drops are slightly higher in the granite fracture for the lowest average velocities, which can be explained by the influence of AD in this region, in which only the channels with the highest aperture are conducting. Moreover, as described by Rodríguez de Castro et al. (2019), the overall flow is a power law of ∇P with an exponent of 1/nrate (for $\nabla P \gg \frac{2\tau_0}{h_0}$ where h_0 is the aperture of the narrowest flow channel in the fracture) when all flow channels are conducting at high pressure gradients. According to the preceding remark, Fig. 7 shows that all the flow channels are conducting at the highest flow rates imposed during the present experiments for both fractures.

It should be noted that porous media and rough-walled rock fractures share the same characteristics in many features. In this regard, Fig. 7 suggests porous media type scaling, displaying the three distinct flow regimes previously reported Bauer et al. (2019): 1) a power-law regime at the lowest flow rates within which the yield stress fluid only flows through the high-conductance channels, 2) an intermediate region in which the yield stress fluid progressively yields in more and more channels as the flow rate is increased and 3) a power law of ∇P with an exponent of 1/n at the highest flow rates, with the yield stress fluid flowing through all channels. Bauer et al. (2019) performed lattice Boltzmann numerical experiments in 3D porous media and laboratory experiments showing that the microstructural disorder of sphere packs and sandstones led to this type of porous media scaling. Also, Chaparian and Tammisola (2020) conducted numerical experiments to analyze the hydrodynamic features of yield-stress fluids flowing through 2D porous media under no-slip and sliding conditions, reporting the same type of porous media scaling in their Q vs. ∇P datasets.

5.4. Experimental results: obtained Aperture Distributions

The experimental data presented in Fig. 7 were used as input to the YSM algorithm, which allowed the determination of the HAD of both rough-walled fractures, as displayed in Fig. 8. It should be noted that the probability distributions represented in Fig. 8 are discrete. Therefore, the relative frequencies of the different aperture classes can be directly obtained from the vertical coordinate value, without calculating the surface area under the curve as in the case of a continuous distribution. The lines joining the symbols represented in the figure are only provided in order to facilitate the reading of the graph. Moreover, the flow curves predicted by the model used in YSM and presented in Subsection 2.2. are provided as supplementary material (Figure S2). The computed peaks of probability were 498 μm for the Vosges sandstone fracture and 914 μm for the granite fracture. Therefore, as shown in Fig. 8, the mode of the inferred HAD is nearly equal to the Newtonian hydraulic aperture for both fractures. However, this conclusion cannot be generalized to all porous medium-yield stress fluid combinations, and differences can
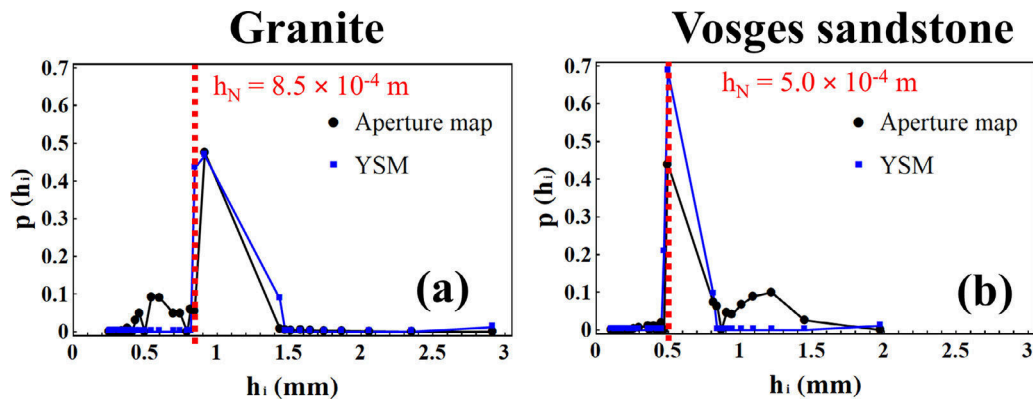
Fig. 8. Hydraulic Aperture Distributions provided by the YSM laboratory experiments presented in Section 4 and comparison to the Aperture Distributions obtained from Fig. 3 (Nowamooz et al. 2013). Blue symbols correspond to the YSM results, while black symbols correspond to the measurements performed by Nowamooz et al. (2013). The vertical dotted lines correspond to the Newtonian hydraulic aperture of each fracture.

be observed in porous media with different microstructural characteristics. This aspect was addressed in a previous work (Rodríguez de Castro et al. 2016), showing that the mode of the pore size distribution provided by YSM and the hydraulic radius of a set of consolidated porous media did not always coincide. In the same manner, the present conclusions cannot be generalized to other rough-walled rock fractures without further investigation. Also, the averages of the HADs provided by YSM were 538 μm for the Vosges sandstone fracture and 953 μm for the granite fracture. These values are close to the Newtonian hydraulic aperture in both cases (Table 2), which is consistent with the numerical results presented in Subsection 5.1. From Fig. 8, it can also be observed that the HADs provided by YSM are quite narrow. Given that YSM provides the hydraulic apertures of the flow channels, a narrow HAD can be interpreted as a quasi-monodisperse size distribution of the flow channels constrictions.

To go further, the results provided by YSM were also compared in Fig. 8 to the Aperture Distributions (ADs) computed from the image-processing procedure performed by Nowamooz et al. (2013). The locations of the bins represented in Fig. 8 correspond to the raw aperture classes defined by Eq. (5) for the YSM experiments under consideration. It should be noted that the density of measurements in the work of Nowamooz et al. (2013) was higher than in the work of Rodríguez de Castro and Radilla (2017) to which YSM method was applied. Therefore, all the original aperture classes of Nowamooz et al. (2013) falling within the range a single bin of the YSM aperture distribution were merged to allow comparison. Independently of YSM results, a first interesting observation is the evident similarity between the ADs provided by the image-processing method for both fractures. Indeed, the average apertures obtained with this method (h_m in Table 2) were 847 μm and 900 μm for the Vosges sandstone fracture and the granite fracture, respectively. Moreover, the range of aperture classes with significant probability is also very close in both fractures (from ~500 μm to ~1500 μm). Therefore, the image-processing method based on the measurement of light intensity through the attenuation law of Beer-Lambert does not directly provide the distribution of hydraulic apertures.

A substantial difference between the results of both methods lies in the dispersion of the computed ADs (image-processing) and HADs (YSM). Indeed, the ADs provided by image-processing are more disperse, which was expected given that this method maps the whole fracture, without any influence of the paths taken by the fluid during injection. However, in the case of the YSM method, the measured quantity is the macroscopic pressure drop. Given that the aperture of the flow path evolves throughout the length of a flow channel, YSM measurements are dominated by the apertures generating the lowest conductance, i.e., the constrictions, as shown in a preceding work (Rodríguez de Castro et al., 2019). Consequently, the frequencies of the greater aperture di-

mensions connected in series with the constrictions throughout the flow path will be absorbed by the presence of a low-conductance zone, resulting in narrower Aperture Distributions for YSM. The contributions to the overall flow rate of a set of four different aperture classes determined by YSM in the case of the Vosges sandstone fracture are provided as supplementary material (Figure S3).

As a consequence of the preceding observations, the HAD provided by YSM method are validated based on the following results:

1) The Newtonian hydraulic aperture of each fracture h_N is close to the average of the HAD provided by YSM for both fractures.
2) The HADs obtained by YSM fall within the range of geometric apertures obtained by Nowamooz for both fractures.
3) The relationships between Q and ∇P are properly represented by the sum of the individual flows through a set of elementary rectangular channels of hydraulic aperture h_i (as can be observed in Figure S3 of the supplementary material), which is consistent with the model presented in Subsection 2.1.
4) The sum of the widths of the individual channels characterized by YSM ($\sum_{i=1}^{z} w_i$) is almost identical to the total width W of the fracture (difference lower than 3% in both cases).

6. Summary and conclusion

The non-toxic Yield Stress porosimetry Method has been extended to the characterization of the Hydraulic Aperture Distribution of rough-walled rock fractures, by adapting the model used to describe the pore space and also the inversion procedure. Then, several 2D direct numerical simulations have been performed in order to interpret the physical meaning of the characterized aperture dimension. Moreover, a set of experimental data has been used to obtain the HADs of two replicas of real rough-walled rock fractures by using YSM, and the results have been compared to the ADs provided by an image-processing technique. The main conclusions can be summarized as follows:

- The HADs of the real fracture replica were successfully obtained by applying the extended version of YSM.
- The probability peaks of the HADs obtained by YSM are very close to the hydraulic apertures for Newtonian flow.
- The whole range of computed aperture sizes falls within the bounds of the ADs determined by an image-processing method.
- The image-processing method does not directly capture the differences in terms of hydraulic aperture between the investigated rough-walled rock fractures. Therefore, this method cannot be directly used to accurately predict the relationships between pressure gradient and injection flow rate, neither for Newtonian fluid neither for non-Newtonian fluids.

Furthermore, the results of the numerical experiments revealed that:

- The HADs computed with YSM from the experimental $(Q_i, \nabla P_i)$ data are close to the distribution of Newtonian hydraulic apertures of the different flow channels.
- The plug of stagnant fluid located in the central part of the flow channels breaks close to the constrictions, forming islands of unyielded fluid.
- The fluid remains unyielded in the corners of the sections with large apertures, and the thickness of the fouling layer decreases as the applied pressure gradient is increased.

The implications of these findings are that YSM can be considered as a potential alternative to the existing methods for HAD characterization. The main advantages are the simplicity of the tests, the fact that the investigated fracture is not destroyed, and the possibility of determining an HAD closely related to flow characteristics. Moreover, the usefulness of YSM in characterizing dislocated media and fractured porous media presenting preferential flow paths has been demonstrated. However, despite the encouraging results discussed above, further experiments are required in order to establish YSM as a reliable porosimetry method for rough-walled fractures. Future studies could fruitfully explore this issue further by characterizing a set of fractures displaying a wide range of HADs. Given that the present study was conducted using the only available experimental dataset in the literature, future works will also provide an opportunity to optimize the experimental procedures of the YSM tests, which should allow for obtaining HADs with more bins in the vicinity of the probability peaks. Also, the development of an efficient manner to produce fracture samples or replicas that can be used in YSM is desirable for future works.

Declaration of Competing Interest

The authors declare that they have no known competing financial interests or personal relationships that could have appeared to influence the work reported in this paper.

Supplementary materials

Supplementary material associated with this article can be found, in the online version, at doi:10.1016/j.advwatres.2020.103794.

References

Ambari, A., Benhamou, M., Roux, S., Guyon, E., 1990. Distribution des tailles des pores d'un milieu poreux déterminée par l'écoulement d'un fluide à seuil. Comptes Rendus de l'Académie des Sciences de Paris 311 (II), 1291–1295.

Auradou, H., Boschan, A., Chertcoff, R., Gabbanelli, S., Hulin, J.P., Ippolito, I., 2008. Enhancement of velocity contrasts by shear-thinning solutions flowing in a rough fracture. J. Non-Newtonian Fluid Mech.153 53–61.

Auradou, H., Drazer, G., Boschan, A., Hulin, J.P., Koplik, J., 2006. Flow channeling in a single fracture induced by shear displacement. Geothermics 35, 576–588.

Bandis, S., 1980. Experimental studies of scale effects on shear strength and deformation of rock joints [Ph.D. thesis]: Leeds, West Yorkshire, England, University of Leeds, 540 p.

Bauer, D., Talon, L., Peysson, Y., Ly, H.B., Batôt, G., Chevalier, T., Fleury, M., 2019. Experimental and numerical determination of Darcy's law for yield stress fluids in porous media. Phys. Rev. Fluids 4, 063301.

Barton, N., Bandis, S., Banktar, K., 1985. Strength, deformation and conductivity coupling of rock joints. Int. J. Rock Mech. Mining Sci. Geomech. Abstracts 22, 121–140.

Berkowitz, B., 2002. Characterizing flow and transport in fractured geological media: A review. Adv. Water Resour.25 861–884.

Berre, I., Doster, F., Keilegavlen, E., 2019. Flow in fractured porous media: a review of conceptual models and discretization approaches. Transport in Porous Media 130 (1), 215–236.

Billaux, D., Gentier, S., 1990. Numerical and laboratory studies of flow in a fracture. In: Barton, W., Stephansson, E. (Eds.), Rock joints: Proceedings of the International Symposium on Rock Joints. A.A. Balkema, Rotterdam, pp. 369–373.

Birdsell, D, Rajaram, H, Viswanathan, DDH, 2015. Hydraulic fracturing fluid migration in the subsurface: a review and expanded modeling results. Water Resour. Res. 37, 1–30.

Boutt, D. F., Grasselli, G., Fredrich, J. T., Cook, B. K., Williams, J. R.: Trapping zones: The effect of fracture roughness on the directional anisotropy of fluid flow and colloid transport in a single fracture: Geophysical Research Letters 33, L21402 (2006).

Bultreys, T., De Boever, W., Cnudde, V., 2016. Imaging and image-based fluid transport modeling at the pore scale in geological materials: A practical introduction to the current state-of-the-art. Earth-Sci. Rev.155 93–128.

Burlion, N., Bernard, D., Chen, D., 2006. X-ray microtomography, Application to microstructure analysis of a cementitious material during leaching process. Cement and Concrete Research 36, 346–357.

Cao, Y., Feng, X., Yan, E., Chen, G., Lü, F., Ji, H., Song, K., 2016. Calculation method and distribution characteristics of fracture hydraulic aperture from field experiments in fractured granite area. Rock Mech. Rock Eng.49 1629–1647.

Chaparian, E., Tammisola, O., 2020. Complex sliding flows of yield stress fluids. arXiv:2004.02950 [physics.flu-dyn].

Chevalier, T., Rodts, S., Chateau, X., Boujlel, J., Maillard, M., Coussot, P., 2013. Boundary layer (shear-band) in frustrated viscoplastic flows. Europhysocs Lett.102 (4) 48002.

Chhabra, R. P., Richardson, J. F., 2008. Non-Newtonian flow and applied rheology: engineering applications. Amsterdam; Boston: Butterworth-Heinemann/Elsevier.

Cieszko, M, Kempinski, M, Czerwinski, T., 2019. Limit models of pore space structure of porous materials for determination of limit pore size distributions based on mercury intrusion data. Transport in Porous Media 127, 433–458.

COMSOL Multiphysics version 5.3. www.comsol.com, COMSOL AB, Stockholm, Sweden (2017).

Committee on Fracture Characterization and Fluid Flow, U.S. National Committee for Rock Mechanics, Geotechnical Board, Board on Energy and Environmental Systems, Commission on Engineering and Technical Systems, and National Research Council, Rock fractures and fluid flow, 1996. Contemporary understanding and applications. National Academies Press, Washington, D.C., p. 568.

Dang, W., Wu, W., Konietzky, H., Qian, J., 2019. Effect of shear-induced aperture evolution on fluid flow in rock fractures. Comp. Geotech.114, 103152.

De Souza Mendes, P.R., Naccache, M.F., Varges, P.R., Marchesini, F.H., 2007. Flow of viscoplastic liquids through axisymmetric expansions–contractions. J. Non-Newtonian Fluid Mech.142 (1–3) 207–217.

Di Cristo, C., Iervolino, M., Moramarco, T., Vacca, A., 2019. Applicability of Kinematic model for mud-flows: An unsteady analysis. J. Hydrol.577, 123967.

Di Federico, V., 1997. Estimates of equivalent aperture for Non-Newtonian flow in a rough-walled fracture. Int. J. Rock Mech. Mining Sci.34 (7) 1133–1137.

Di Federico, V., 1998. Non-Newtonian flow in a variable aperture fracture. Transport in Porous Media 30 (1), 75–86.

Doube, M., Kłosowski, M.M., Arganda-Carreras, I., Cordelières, F.P., Dougherty, R.P., Jackson, J.S., Schmid, B., Hutchinson, J.R., Shefelbine, S.J., 2010. BoneJ: Free and extensible bone image analysis in ImageJ. Bone 47 (6), 1076–1079.

Ferrás, L.L., Nóbrega, J.M., Pinho, F.T., 2012. Analytical solutions for Newtonian and inelastic non-Newtonian flows with wall slip. J. Non-Newtonian Fluid Mech.175 –176, 76–88.

Felisa, G., Lenci, A., Lauriola, I., Longo, S., Di Federico, V., 2018. Flow of truncated power law fluid in fracture channels of variable aperture. Adv. Water Resour.122 317–327.

Forey, N., Atteia, O., Omari, A., Bertin, H., 2020. Saponin foam for soil remediation: On the use of polymer or solid particles to enhance foam resistance against oil. J. Contam. Hydrol.228, 103560.

Frigaard, I.A., Nouar, C., 2005. On the usage of viscosity regularisation methods for visco-plastic fluid flow computation. J. Non-Newtonian Fluid Mech.127 (1) 1–26.

Frigaard, I, Paso, K, de Souza Mendes, P., 2017. Bingham's model in the oil and gas industry. Rheologica Acta 56, 259–282.

Frigaard, I.A., Ryan, D.P., 2004. Flow of a visco-plastic fluid in a channel of slowly varying width. J. Non-Newtonian Fluid Mech.123 67–83.

Gale, J.E., 1987. Comparison of coupled fracture deformation and fluid flow models with direct measurements of fracture pore structure and stress-flow properties. A.A. Balkema, Rotterdam, pp. 1213–1222.

Giesche, H., 2006. Mercury Porosimetry: a General (Practical) Overview. Particle & Particle Systems Characterization 23, 1–11.

Glover, P.W.J., Matsuki, K., Hikima, R., Hayashi, K., 1998. Fluid flow in synthetic rough fractures and application to the Hachimantai geothermal HDR test site. J. Geophys. Res.103 9621–9635.

Hakami, E., Einstein, H.H., Gentier, S., Iwano, M., 1995. Characterization of fracture apertures – methods and parameters. In: Proceedings of the Eighth International Congress on Rock Mechanics, September 1995, II. Tokyo, pp. 751–754.

Hewitt, D.R., Daneshi, M., Balmforth, N.J., Martinez, D.M., 2016. Obstructed and channelized Viscoplastic flow in a Hele-Shaw cell. J. Fluid Mech.790 173–204.

Houston, A.N., Otten, W., Falconer, R., Monga, O., Baveye, P.C., Hapca, S.M., 2017. Quantification of the pore size distribution of soils: Assessment of existing software using tomographic and synthetic 3D images. Geoderma 299, 73–82.

Huo, D., Pini, R., Benson, S.M., 2016. A calibration-free approach for measuring fracture aperture distributions using X-ray computed tomography. Geosphere 12, 558–571.

Isakov, E., Ogilvie, S.R., Taylor, C.W., Glover, P.W., 2001. Fluid flow through rough fractures in rocks I: high resolution aperture determinations. Earth Planet. Sci. Lett.191 (3–4) 267–282.

Javadi, M., Sharifzadeh, M., Shahriar, K., 2010. A new geometrical model for non-linear fluid flow through rough fractures. J. Hydrol.389 18–30.

Johns, R.A., Steude, J.S., Castanier, L.M., Roberts, P.V., 1993. Nondestructive measurements of fracture aperture in crystalline rock cores using X ray computed tomography. J. Geophys. Res.98 (B2) 1889–1900.

Karpyn, Z.T., Grader, A.S., Halleck, P.M., 2007. Visualization of fluid occupancy in a rough fracture using micro-tomography. J. Colloid Interface Sci.307 181–187.

Karpyn, Z., Landry, C., Prodanovic, M., 2016. Induced rough fracture in Berea sandstone core. Digital Rocks Portal. [Online]. Available http://www.digitalrocksportal.org. [Assessed: 8-Jan-2020].

Ketcham, R.A., Carlson, W.D., 2001. Acquisition, optimization and interpretation of X-ray computed tomographic imagery: Applications to the geosciences. Comp. Geosci.27 381–400.

Kovscek, A.R., Bertin, H.J., 2003. Foam mobility in heterogeneous porous media. Transport in Porous Media 52, 17–35.

Lai, J., Wang, G., Fan, Z., Chen, J., Qin, Z., Xiao, C., Wang, S., Fan, X., 2017. Three-dimensional quantitative fracture analysis of tight gas sandstones using industrial computed tomography. Sci. Rep.7 1825.

Lavrov, A., 2013a. Non-Newtonian fluid flow in rough-walled fractures: A brief review. In: Proceedings of ISRM SINOROCK 2013, 18–20 June, Shanghai, China Int. Soc. for Rock Mech. Lisboa, Portugal.

Lavrov, A., 2013b. Redirection and channelization of power-law fluid flow in a rough-walled fracture. Chem. Eng. Sci.99 81–88.

León y León, C.A., 1998. New perspectives in mercury porosimetry. Adv. Colloid and Interface Sci. 76–77, 341–372.

Li, Z., Liu, D., Cai, Y., Ranjith, P.G., Yao, Y., 2017. Multi-scale quantitative characterization of 3-D pore-fracture networks in bituminous and anthracite coals using FIB-SEM tomography and X-ray μ-CT. Fuel 209, 43–53.

Li, B., Mo, Y., Zou, L., Liu, R., Cvetkovic, V., 2020. Influence of surface roughness on fluid flow and solute transport through 3D crossed rock fractures. J. Hydrol.582, 124284.

Lindquist, W.B., Venkatarangan, A., 2000. Pore and throat size distributions measured from synchrotron X-ray tomographic images of Fontainebleau sandstones. J. Geophys. Res. Solid Earth 105 (B9), 21509–21527.

Malvault, G., 2013. Détermination expérimentale de la distribution de taille de pores d'un milieu poreux par l'injection d'un fluide à seuil ou par analyse fréquentielle, PhD thesis, Arts et Métiers ParisTech.

Mitsoulis, E., Huilgol, R.R., 2004. Entry flows of Bingham plastics in expansions. J. Non-Newtonian Fluid Mech. 122, 45–54.

Morris, J.P., Chochua, G.G., Bogdan, A.V., 2015. An efficient non-Newtonian fluid-flow simulator for variable aperture fractures. Can. J. Chem. Eng.93 (11) 1902–1915.

Neuzil, C.E., Tracy, J.V., 1981. Flow through fractures. Water Resour. Res. 17 (1), 191–199.

Nowamooz, A., Radilla, G., Fourar, M., Berkowitz, B., 2013. Non-Fickian transport in transparent replicas of rough-walled rock fractures. Transport in Porous Media 98 (3), 651–682.

Omirbekov, S., Davarzani, H., Colombano, S., Ahmadi-Sénichault, A., 2020. Experimental and numerical upscaling of foam flow in highly permeable porous media. Adv. Water Resour..

Oukhlef, A., 2011. Détermination de la distribution de tailles de pores d'un milieu poreux, PhD thesis, Arts et Métiers ParisTech.

Oukhlef, A., Champmartin, S., Ambari, A., 2014. Yield stress fluids method to determine the pore size distribution of a porous medium. J. Non-Newtonian Fluid Mech.204 87–93.

Prodanovic, M., Lindquist, W.B., Seright, R.S., 2006. Porous structure and fluid partitioning in polyethylene cores from 3D X-ray microtomographic imaging. J. Colloid and Interface Sci.298 282–297.

Pyrak-Nolte, L. J., Myer, L. R., Cook, N. G., Witherspoon, R. A., 1987. Hydraulic and mechanical properties of natural fractures in low permeability rock, Proceedings, 6th International Society of Rock Mechanics Congress: Rotterdam, A.A. Balkema, p. 225–232.

Rodríguez de Castro, A.: Flow Experiments of Yield Stress Fluids in Porous Media As a New Porosimetry Method. PhD thesis, Arts et Métiers ParisTech (2014)

Rodríguez de Castro, A., Agnaou, A., 2019. Numerical investigation of the apparent viscosity dependence on darcy velocity during the flow of shear-thinning fluids in porous media. Transport in Porous Media 129 (1), 93–120.

Rodríguez de Castro, A., Agnaou, M., Ahmadi-Sénichault, A., Omari, A., 2019. Application of non-toxic Yield Stress fluids porosimetry Method and Pore-Network Modelling to characterize the Pore Size Distribution of packs of spherical beads. Transport in Porous Media 130 (3), 799–818.

Rodríguez de Castro, A., Agnaou, M., Ahmadi-Sénichault, A., Omari, A., 2020. Numerical porosimetry: Evaluation and comparison of Yield Stress fluids Method, Mercury Intrusion Porosimetry and pore Network Modelling approaches. Comp. Chem. Eng.133, 106662.

Rodríguez de Castro, A., Ahmadi-Sénichault, A., Omari, A., Savin, S., Madariaga, L.-F., 2016. Characterizing porous media with the Yield Stress Fluids porosimetry Method. Transport in Porous Media 114 (1), 213–233.

Rodríguez de Castro, A., Ahmadi-Sénichault, A., Omari, A., 2018. Using xanthan gum solutions to characterize porous media with the yield stress fluid porosimetry method: robustness of the method and effects of polymer concentration. Transport in Porous Media 122 (2), 357–374.

Rodríguez de Castro, A., Omari, A., Ahmadi-Sénichault, A., Bruneau, D., 2014. Toward a new method of porosimetry: principles and experiments. Transport in Porous Media 101 (3), 349–364.

Rodríguez de Castro, A., Radilla, G., 2017. Flow of yield stress and Carreau fluids through rough-walled rock fractures: Prediction and experiments. Water Resour. Res.53 6197–6217.

Roustaei, A., Chevalier, T., Talon, L., Frigaard, I.A., 2016. Non-Darcy effects in fracture flows of a yield stress fluid. J. Fluid Mech.805 222–261.

Roustaei, A., Frigaard, I.A., 2013. The occurrence of fouling layers in the flow of a yield stress fluid along a wavy-walled channel. J. Non-Newtonian Fluid Mech.198 109–124.

Schindelin, J., Arganda-Carreras, I., Frise, E., Kaynig, V., Longair, M., Pietzsch, T., Preibisch, S., Rueden, C., Saalfeld, S., Schmid, B., Tinevez, J.-Y., White, D.J., Hartenstein, V., Eliceiri, K., Tomancak, P., Cardona, A., 2012. Fiji: an open-source platform for biological-image analysis. Nature Methods9 (7) 676–682.

Schrauf, T.W., Evans, D.D., 1986. Laboratory studies of gas flow through a single natural fracture:. Water Resour. Res.22 1038–1050.

Skelland, A.H.P., 1967. Non-Newtonian Flow and Heat Transfer. Wiley, New York.

Shojaei, M.J., Rodríguez de Castro, A., Méheust, Y., Shokri, N., 2019. Dynamics of foam flow in a rock fracture: Effects of aperture variation on apparent shear viscosity and bubble morphology. J. Colloid and Interface Sci.552 464–475.

Silva, J.A.K., Smith, M.M., Munakata-Marr, J., McCray, J.E., 2012. The effect of system variables on in situ sweep-efficiency improvements via viscosity modification. J. Contam. Hydrol.136 –137, 117–130.

Tembely, M., AlSumaiti, A.M., Rahimov, K., Jouini, M.S., 2019. Pore-Scale Modeling of Non-Newtonian Fluid Flow Through Micro-CT Images of Rocks. In: Ao SI., Gelman, L., Kim, H. (Eds.), Transactions on Engineering Technologies. WCE 2017. Springer, Singapore.

Tsang, Y.W., 1992. Usage of "equivalent apertures" for rock fractures as derived from hydraulic and tracer tests. Water Resour. Res.28 1451–1455.

Tsang, Y.W., Tsang, C.F., 1987. Channel model of flow through porous media. Water Resour. Res.23 (3) 467–479.

Voorn, M., Exner, U., Barnhoorn, A., Baud, P., Reusché, T., 2015. Porosity, permeability and 3D fracture network characterisation of dolomite reservoir rock samples. J. Petrol. Sci. Eng.127 270–285.

Weerakone, W.M.S.B, Wong, R.C.K., 2010. Characterization of variable aperture rock fractures using X-ray computer tomography. In: Desrues, J., Viggiani, G., Bésuelle, P. (Eds.), Advances in X-ray Tomography for Geomaterials. https://doi.org/10.1002/9780470612187.ch21.

Wildenschild, D., Sheppard, A.P., 2012. X-ray imaging and analysis techniques for quantifying pore-scale structure and processes in subsurface porous medium systems. Adv. Water Resour.51 217–246.

Zhang, M., Prodanovic, M., Mirabolghasemi, M., Zhao, J., 2019. 3D microscale flow simulation of shear-thinning fluids in a rough fracture. Transport in Porous Media 128 (1), 243–269 (2019).